

Oxygen vacancies and hydrogen doping in LaAlO₃/SrTiO₃ heterostructures: electronic properties and impact on surface and interface reconstruction

I. I. Piyanzina,^{1,2} V. Eyert,³ Yu. V. Lysogorskiy,² D. A. Tayurskii,² and T. Kopp¹

¹*Center for Electronic Correlations and Magnetism,*

Institute of Physics, University of Augsburg, 86135 Augsburg, Germany

²*Institute of Physics, Kazan Federal University, 420008 Kazan, Russia*

³*Materials Design SARL, 42 Avenue Verdier, 92120 Montrouge, France*

(Dated: April 19, 2019)

We investigate the effect of oxygen vacancies and hydrogen dopants at the surface and inside slabs of LaAlO₃, SrTiO₃, and LaAlO₃/SrTiO₃ heterostructures on the electronic properties by means of electronic structure calculations as based on density functional theory. Depending on the concentration, the presence of these defects in a LaAlO₃ slab can suppress the surface conductivity. In contrast, in insulating SrTiO₃ slabs already very small concentrations of oxygen vacancies or hydrogen dopant atoms induce a finite occupation of the conduction band. Surface defects in insulating LaAlO₃/SrTiO₃ heterostructure slabs with three LaAlO₃ overlayers lead to the emergence of interface conductivity. Calculated defect formation energies reveal strong preference of hydrogen dopant atoms for surface sites for all structures and concentrations considered. Strong decrease of the defect formation energy of hydrogen adatoms with increasing thickness of the LaAlO₃ overlayer and crossover from positive to negative values, taken together with the metallic conductivity induced by hydrogen adatoms, seamlessly explains the semiconductor-metal transition observed for these heterostructures as a function of the overlayer thickness. Moreover, we show that the potential drop and concomitant shift of (layer resolved) band edges is suppressed for the metallic configuration. Finally, magnetism with stable local moments, which form atomically thin magnetic layers at the interface, is generated by oxygen vacancies either at the surface or the interface, or by hydrogen atoms buried at the interface. In particular, oxygen vacancies in the TiO₂ interface layer cause drastic downshift of the 3d *e_g* states of the Ti atoms neighboring the vacancies, giving rise to strongly localized magnetic moments, which add to the two-dimensional background magnetization.

I. INTRODUCTION

Oxide heterostructures have been in the focus of solid state research for more than a decade.^{1–3} The intense exploration of the multilayered systems is well justified as electronic reconstruction^{4–6} at the internal interfaces and the surfaces allows for a plethora of phenomena which are otherwise not observed in a single compound. Moreover, the sensitivity of competing or even coexisting phases to external fields and control parameters in the transition metal oxides makes the oxide heterostructures ideal candidates for multifunctional devices – especially since metallic phases may be confined to thin sheets with a thickness of a few lattice constants.

For the paradigmatic oxide heterostructure with LaAlO₃ (LAO) thin films on SrTiO₃ (STO) substrates,^{7,8} distinct electronic phases have been extensively characterized at the LAO-STO interface: for LAO films with more than 3 layers⁹ and LaO termination towards the TiO₂ interface, a nm-wide¹⁰ metallic^{7,9} state is formed in the STO layers next to the interface which becomes superconducting below a temperature of approximately 300 mK.¹¹ Remarkably, the superconducting state coexists with a magnetic state possibly formed in patches of an inhomogeneous interface state.^{12,13} The magnetism¹⁴ appears to be stable up to room temperature but its origin has not been settled.^{15–22} It may be well related to oxygen vacancies^{16,19,20,23,24} at the interface and/or the surface which lead to an orbital reconstruction of

nearby Ti sites and generate a local spin polarization. The orbital reconstruction involves a splitting of the Ti 3d *e_g* states on account of an oxygen vacancy in the vicinity of the Ti interface site. The *e_g* orbital with a lobe in the direction of the vacancy position is lowered energetically so substantially that it is partially occupied and Hund's coupling induces magnetic moment formation.¹⁶ Other scenarios such as the formation of Ti³⁺-on-Al³⁺ defects in LAO near the interface²² or the Zener exchange between an insulating interface layer and the nearest TiO₂ plane have been suggested.^{17,25} Importantly, Rashba spin-orbit coupling is generated at the interface^{26,27} through inversion symmetry breaking which leads to anomalous magnetotransport^{26,28–31} and may even stabilize non-trivial topological states.^{32–35} Moreover, capacitance measurements reveal that the electronic compressibility at the interface can be negative for low charge carrier concentration (controlled by a sufficiently large negative bias).³⁶ It is not yet decided if the negative compressibility originates from interaction effects,^{36–38} strong spin-orbit coupling,^{39,40} or from the electronic reconstruction in multiple planes.⁴¹ Eventually, the dielectric properties of the heterostructure control electronic transport, and strain has a strong impact on them.⁴² Electrostrictive and flexoelectric coupling on the STO side may play an important role in explaining the abruptness of the Lifshitz transition between low and intermediate electron density at the interface.⁴³ Electronic devices from oxide interfaces are now feasible: cir-

cuits with all-oxide field-effect transistors were fabricated from LAO/STO heterostructures.⁴⁴ Recent progress in the fabrication of multilayered systems allows to manufacture stable polar nanostructures⁴⁵ and to make use of their respective functionalities.

With all these striking findings the electronic reconstruction at the LAO-STO interface is not yet profoundly understood. The polar catastrophe mechanism, in which half an electron per planar unit cell is transferred from the surface to the interface, can neither account for the insulating surface state^{9,46} nor the sizable suppression of the internal electrostatic field in the LAO film⁴⁷⁻⁴⁹ nor the built-up of a similar (superconducting) metallic interface state in samples where the polar LAO was replaced by amorphous aluminium oxide.⁵⁰

In this respect, the question arises if defect states play an important role, especially if they are electron donor states.^{16,22,49,51-54} Also the debate concerning the origin of magnetism motivates to investigate defect states. Although defects are often considered to be unavoidable “dirt” they nevertheless can decisively influence the electronic reconstruction at surfaces and interfaces and thereby contribute to their functionalization. However, we are still lacking a comprehensive account of the electronic reconstruction in the presence of defects. Certainly, this is beyond the scope of a single investigation. Here, we resort to first principles calculations and focus on oxygen vacancies and hydrogen dopants with the motivation that they are omnipresent and are both electron donors. The defect states have been analyzed before and a good understanding about their role in forming a conducting LAO-STO interface in conjunction with an insulating LAO surface is being developed.^{16,22,51-54} Here, we address defect profiles through the entire heterostructure and reconsider orbital reconstruction of the Ti 3*d* states with the formation of sizable magnetic moments. The essential issue is to understand the impact of defects on the interface electronic states.

The paper is organized as follows: In Sec. II we briefly discuss our approach to model the perovskite slabs as well as the LAO-STO heterostructure and introduce the computational method that we employ in the presence of defects. We present the results on the electronic structure and defect formation energies in dependence on hydrogen adatoms and oxygen vacancies in LAO and STO slabs, and in LAO-STO heterostructures in subsections III A, III B and, III C, respectively. In the last part of III C, we discuss the consequences of surface passivation through hydrogen atoms, in particular the appearance of an insulating surface state in the presence of a conducting interface, the absence of a potential built-up in the LAO overlayers and a critical thickness of the LAO film. In Sec. IV we review the formation of local magnetic moments and orbital reconstruction through oxygen vacancies and introduce a magnetic state with hydrogen defects at the the interface of the LAO-STO heterostructure. Sec. V summarizes our results.

II. COMPUTATIONAL METHOD

The *ab initio* calculations were based on density functional theory (DFT).^{55,56} Exchange and correlation effects were accounted for by the generalized gradient approximation (GGA) as parametrized by Perdew, Burke, and Ernzerhof (PBE).⁵⁷ The Kohn-Sham equations were solved with projector-augmented-wave (PAW) potentials and wave functions⁵⁸ as implemented in the Vienna Ab-Initio Simulation Package (VASP),⁵⁹⁻⁶¹ which is part of the MedeA[®] software of Materials Design.⁶² Specifically, we used a plane-wave cutoff of 400 eV. The force tolerance was 0.05 eV/Å and the energy tolerance for the self-consistency loop was 10^{-5} eV. The Brillouin zones were sampled using Monkhorst-Pack grids⁶³ including $5 \times 5 \times 1$ **k**-points in case of the 2×2 supercells of LaAlO₃ and SrTiO₃ slabs. In contrast, for the heterostructures with their increased number of atoms we used $3 \times 6 \times 1$ **k**-points for the 2×1 supercells and $3 \times 3 \times 1$ **k**-points for the 2×2 supercells. Finally, the electronic densities of states were calculated using the linear tetrahedron method⁶⁴ on $4 \times 4 \times 1$ **k**-point grids.

All calculations were performed in the framework of the GGA+*U* method using the simplified approach proposed by Dudarev *et al.*,⁶⁵ which takes only the difference of $U - J$ into account. We applied additional local correlations of $U - J = 8$ eV and $U - J = 2$ eV to the La 4*f* and the Ti 3*d* orbitals, respectively. This choice is based on our previous detailed investigation of the effect of local electronic correlations as captured by the GGA+*U* method.⁶⁶ In that study we performed a systematic variation of the $U - J$ values for the aforementioned two orbitals and their effect on the atomic and electronic structure, which led us to conclude that the above values represent good choices and thereby allow for an accurate and at the same time efficient assessment of the systems under study. This conclusion was also supported by our previous work using the GGA+*U* method and the hybrid functional approach.^{67,68}

In order to study the LaAlO₃ and SrTiO₃ surfaces, slabs were constructed comprising $6\frac{1}{2}$ unit cells stacked along the [001] direction and identical termination on both sides (AlO₂ for LaAlO₃ and TiO₂ for SrTiO₃). While the atomic positions of the outer parts of these slabs were allowed to relax, the central region of $1\frac{1}{2}$ unit cells was kept fixed in order to simulate the bulk structure.^{69,70}

The heterostructures were modeled by a central region of SrTiO₃ comprising $4\frac{1}{2}$ unit cells with TiO₂ termination on both sides and three LaAlO₃ overlayers with LaO termination towards the central slab and AlO₂ surface termination also on both sides (see Fig. 4 of Ref. 71). This slab model guaranteed a non-polar structure without any artificial dipoles. Finally, in order to avoid interaction of the surfaces and slabs with their periodic images, 20 Å-wide vacuum regions were added in accordance with previous work.^{68,71} The in-plane lattice parameter $a = b = 3.905$ Å was fixed to the experimental

values of bulk SrTiO₃⁷ and kept for all subsequent calculations reflecting the stability of the substrate. However, in contrast to the pure LAO and STO slabs mentioned in the previous paragraph in the heterostructure with its thinner STO core the atomic positions of all atoms were fully relaxed.

In passing we mention that throughout in this paper the term heterostructure refers to slab models of the kind just described, in particular, with a wide vacuum region separating the slabs, rather than a structures with infinite alternation of LaAlO₃ and SrTiO₃ slabs.

Finally, to study the influence of defects we used 1×1 , 1×2 and 2×2 in-plane supercells of the above cells. Both oxygen vacancies and hydrogen dopants were introduced at the surface or in a subsurface layer on both sides while preserving the inversion symmetry of the slabs. Defect formation energies were calculated following the standard procedure adopted by many authors.⁷²⁻⁷⁷ Specifically, the oxygen vacancy formation energy E_{form} is defined as

$$E_{\text{form}} = (E_{\text{total}} - (E_{\text{bare}} - n\mu_{\text{O}}(T, p))) / n, \quad (1)$$

where n is the number of vacancies per unit cell. E_{bare} and E_{total} are the total energies of the bare and oxygen-deficient slab, respectively. Finally, $\mu_{\text{O}}(T, p)$ denotes the chemical potential of oxygen, which depends on temperature and oxygen partial pressure. However, the oxygen chemical potential is confined by lower and upper limits reflecting the stability of the system involved. In particular, in the ‘‘oxygen-poor limit’’, where the chemical potential is low, oxygen would start to dissociate and thereby destabilize the slab. In contrast, in the ‘‘oxygen-rich limit’’, oxygen would start to form a condensed O₂ solid phase covering the surface. At ambient conditions both limits are out of reach and a reasonable choice for the upper limit is

$$\mu_{\text{O}}(T, p) = \frac{1}{2}E_{\text{O}_2}, \quad (2)$$

where E_{O_2} is the total energy of a free, isolated O₂ molecule at $T = 0$ K.⁷²⁻⁷⁸ Note that the total energy of the oxygen molecule was determined from spin-polarized calculations.

Similarly, the hydrogen-dopant formation energy E_{form} is given by

$$E_{\text{form}} = (E_{\text{total}} - (E_{\text{bare}} + n\mu_{\text{H}}(T, p))) / n, \quad (3)$$

where n is the number of dopant atoms per unit cell. E_{total} is the total energy of the slab with dopant atoms symmetrically added on both sides, whereas $\mu_{\text{H}}(T, p)$ denotes the chemical potential of hydrogen. As for the case of oxygen, the latter is restricted to a certain range in order to preserve the thermodynamic stability of the slab. Again following the literature, we here resort to the choice

$$\mu_{\text{H}}(T, p) = \frac{1}{2}E_{\text{H}_2}, \quad (4)$$

where E_{H_2} is the total energy of a free, isolated H₂ molecule at $T = 0$ K obtained from spinpolarized calculations.⁷²⁻⁷⁸

In the present context it is important to note that although the aforementioned defects may not even be thermodynamically stable at experimentally accessible conditions, they may nevertheless be created during the synthesis of samples and kinetically frozen. Yet, the above relations may still serve as a means to access the relative stability of defects located at different layers.

III. IMPACT OF IMPURITIES ON STRUCTURES AND ELECTRONIC PROPERTIES

A. LaAlO₃ slab

Bulk LaAlO₃ is a wide gap insulator with a band gap of 5.6 eV and crystallizing in the perovskite structure.⁷ It is used as a high- κ gate dielectric for the recessed-gate GaN MOSFET transistors,⁷⁹ as a substrate for high- T_c superconductors,⁸⁰ and it exhibits colossal magnetoresistance.⁸¹ Recent findings suggest a two-dimensional electron gas at the LaAlO₃ surface, depending on the localization of electrons or holes generated by defects.⁷⁸

The structures of the bare AlO₂-terminated LaAlO₃ slab and the same slab with a hydrogen adatom are shown in Fig. 1. The corresponding top views of 2×2 surface supercells of the bare slab and slabs with different kinds of defects are displayed in Fig. 2 together with the calculated partial electronic densities of states. Obviously, the bare LaAlO₃ surface, while still showing the large separation between O $2p$ and La $5d$ states, which causes the insulating behavior in the bulk material, exhibits metallic behavior due a small fraction of unoccupied O $2p$ bands as has been also found by Krishnaswamy *et al.*⁷⁰ as well as by Silva and Dalpian.⁷⁸ These states arise from the dangling bonds of the orbitals at the surface, which introduce a metallic surface layer. The situation can be understood within a simple ionic picture, where LaAlO₃ is considered as an alternating sequence of charged (AlO₂)⁻ and (LaO)⁺ layers. Thus, formally each LaO layer provides half an electron to the AlO₂ layer below and above such that all atomic shells are completely filled. This ionic model is sketched in Fig. 1 for a 2×2 surface unit cell. Since at the surface this perfect compensation scheme is interrupted, the terminating AlO₂ layer misses two electrons (per 2×2 surface unit cell) to completely fill its O $2p$ states and metallic conductivity equivalent to hole doping arises.

The electronic charge in the surface layer needed to restore insulating behavior can be provided by two hydrogen adatoms or a single oxygen vacancy per 2×2 surface unit cell. These two cases are displayed in Figs. 2(c) and 2(d). According to the corresponding calculated densities of states the proper amount of these defects thus leads to

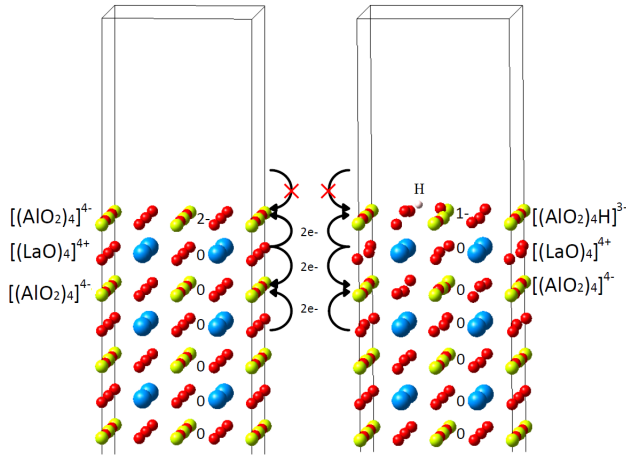


FIG. 1: Structures and ionic models of a bare LaAlO_3 slab (left) and a slab with one hydrogen adatom per 2×2 surface unit cell (right). In both cases the surface is charged but the charge concentrations differ. In contrast, one oxygen vacancy or two hydrogen atoms (per 2×2 surface cell) will result in full charge compensation and insulating states. Only the upper part of the slab is displayed. Arrows indicate electron transfer from LaO planes to the neighboring AlO_2 planes. The surfaces lack two (bare surface) and one (for one H adatom) electron. The formal charge transfers of the 2×2 stacked planar cells are marked in the center of the plot between the two structures.

a complete filling of the O $2p$ states and recovery of the insulating behavior seen in bulk LaAlO_3 as has been also observed by Krishnaswamy and coworkers.⁷⁰ The ionic model displayed in Fig. 1 indicates that in the case of hydrogen adatoms the surface layer now can be formally written as $[(\text{AlO}_2)_4\text{H}_2]^{2-}$, whereas the layers below arise as alternating $[(\text{LaO})_4]^{4+}$ and $[(\text{AlO}_2)_4]^{4-}$ as before. The hydrogen adatoms thus offer two electrons, which in a perfect crystal would be provided by the neighboring LaO layer and thereby restore the insulating behavior at the surface. The same effect is achieved by a single oxygen vacancy.

Finally, the case of only one hydrogen adatom per 2×2 surface unit cell at the surface as shown in Fig. 2(b) or an oxygen vacancy filled by one hydrogen atom as displayed in Fig. 2(e) are intermediate between the situations discussed above. Even though they both cause lowering of the O $2p$ dominated bands, these states are still not completely filled and metallic behavior remains. Within the ionic model the top layers can be formally written as $[(\text{AlO}_2)_4\text{H}_2]^{1-}$ in case of a single hydrogen adatom, i.e. these layers are missing one electron to completely fill the atomic O $2p$ shell.

According to layer-resolved analysis of the partial densities of states of the bare LaAlO_3 surface the O $2p$ contribution at the Fermi energy drops from 10 states/eV in the surface layer to 2 states/eV in the second and third layer. In contrast, oxygen vacancies cause insulating behavior. However, with the vacancies filled by a single

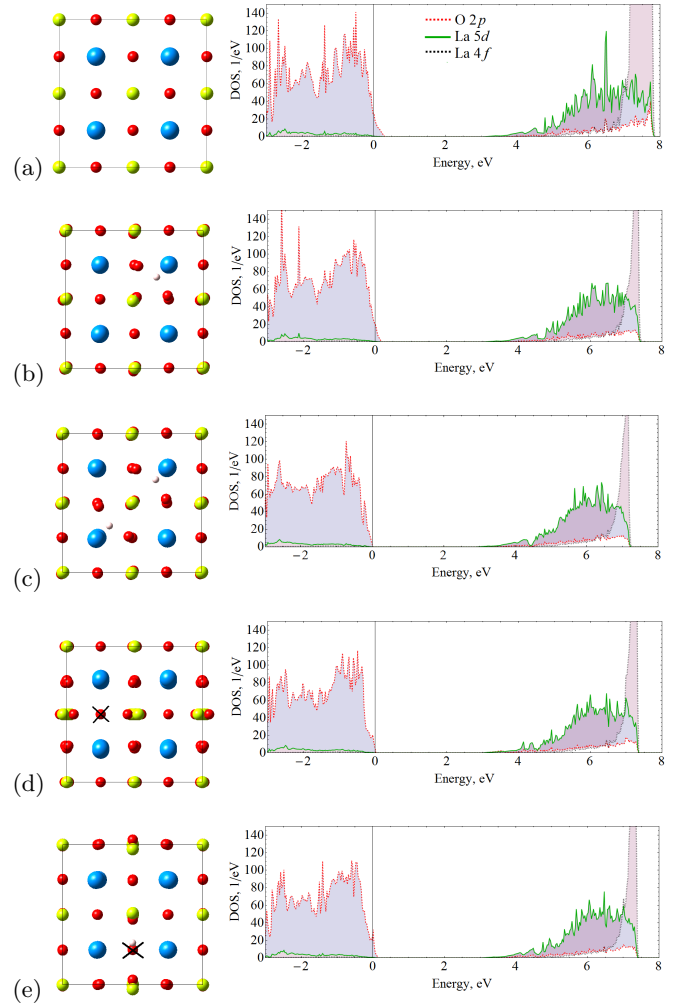


FIG. 2: Left column: top views of (a) bare 2×2 LaAlO_3 surface as well as a surface with (b) one hydrogen atom, (c) two hydrogen atoms, (d) an oxygen vacancy, and (e) an oxygen vacancy filled with a hydrogen atom. Aluminum, lanthanum, oxygen, and hydrogen atoms are given in yellow, blue, red, and light grey, respectively, whereas oxygen vacancies are marked by a cross. Right column: Corresponding partial electronic densities of states.

hydrogen atom the O $2p$ contribution at the Fermi energy drops from about 9 states/eV for the surface layer to 4 states/eV in the second and third layers indicating an increased thickness of the metallic surface layer as compared to the bare surface.

Calculated energies of defect formation are displayed in Fig. 3 for both oxygen vacancies and hydrogen dopant atoms at different concentrations as mimicked by different surface unit cells. In addition, the case of an oxygen vacancy filled with a single hydrogen atom was considered. The corresponding curve was included in both subfigures and serves as an orientation. All defects were placed at different layers ranging from the surface layer to the layer next to the center of the slab. Obviously, positions at the surface are preferred over positions well

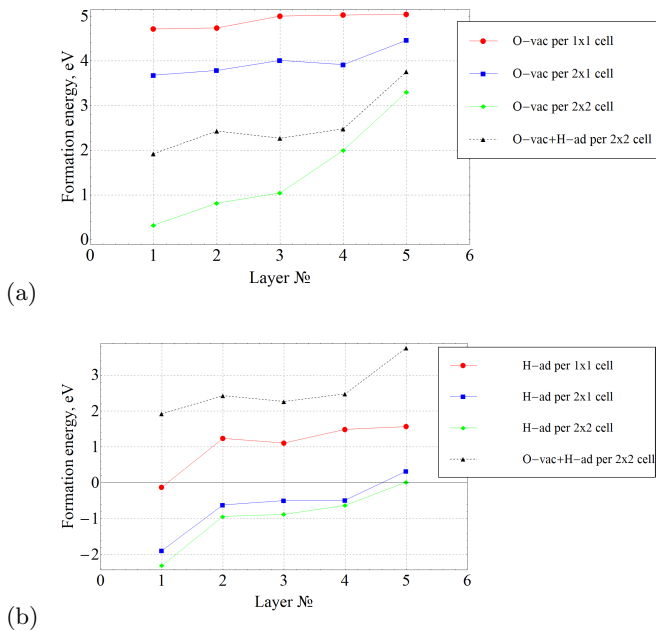


FIG. 3: Defect formation energies of AlO₂-terminated LaAlO₃ slabs (a) with an oxygen vacancy and (b) with a hydrogen dopant atom in dependence of the position of the defect. Layer 1 is the surface layer and counting of layers treats LaO and AlO₂ layers separately.

inside the slab. This trend is most clear for the case of an oxygen vacancy in a 2×2 surface unit cell, which has been also considered by Silva and Dalpian.⁷⁸ Specifically, these authors find an increase of the formation energy of an oxygen vacancy from about 0.3 eV for a vacancy at the surface to about 3.5 eV for a vacancy in the fifth layer in almost perfect agreement with our results. Note that due to the Coulomb repulsion between neighboring defects the energies of defect formation show a strong increase with increasing defect concentration. Finally, we point to the negative formation energy for hydrogen dopant atoms at low concentrations indicating the likelihood of hydrogen adsorption restoring the insulating behavior at the surface.

B. SrTiO₃ slab

SrTiO₃ is an insulator with a gap of 3.2 eV. Like LaAlO₃ it crystallizes in the perovskite structure and is widely used as a substrate for growing thin films as well as in electronic devices such as ceramic capacitors and variable resistors. However, these devices turned out to be affected by hydrogen adsorption due to the dissociation of adsorbed water.^{69,82} This tendency was confirmed by DFT calculations and surface metallicity induced by electron donation from hydrogen was suggested.⁶⁹ Oxygen vacancies can also affect the electrical properties. The emergence of a two-dimensional electron system at

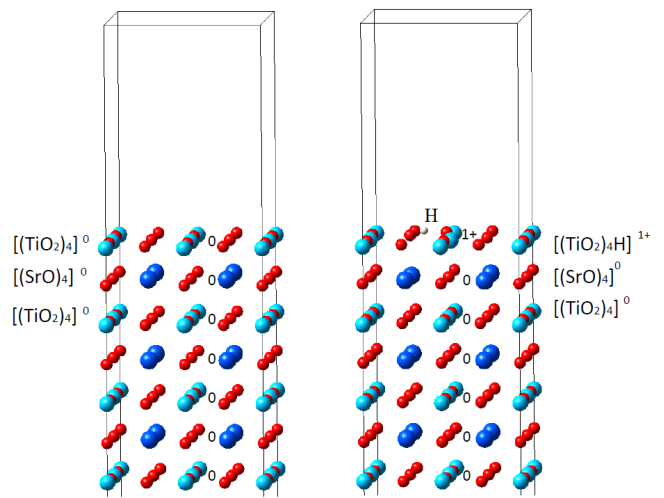


FIG. 4: Structures and ionic models of a bare SrTiO₃ slab (left) and a slab with one hydrogen adatom per 2×2 surface unit cell (right). Within the ionic model there is no charge transfer between layers and hydrogen adatoms and oxygen vacancies at the surface act as electron donors causing finite surface conductivity. Only the upper part of the slab is displayed.

a vacuum-cleaved SrTiO₃ surface was observed in angle-resolved photoelectron spectroscopy.^{83,84} First principles calculations gave evidence that such a two-dimensional electron gas can be generated by oxygen vacancies at the surface.^{85,86} Moreover, electronic correlations were investigated within DFT+DMFT for oxygen-deficient SrTiO₃ surfaces.⁸⁷ Recently, the density of oxygen vacancies at SrTiO₃ surfaces was adjusted in situ during photoemission experiments.⁸⁸ Most prominently, electronic phase separation was identified with a highly doped metallic and insulating or lowly doped phase.⁸⁸ The authors concluded that, most likely, this inhomogeneity is driven chemically by clustering of oxygen vacancies.

The structures of the bare TiO₂-terminated SrTiO₃ slab and the same slab with a hydrogen adatom are displayed in Fig. 4. Hydrogen atoms are adsorbed close to oxygen with bond lengths of 0.986 Å and 0.982 Å, respectively, found for the 2×1 and 2×2 surface models in good agreement with previous observations.⁶⁹ Top views and calculated densities of states for the bare slab and slabs with the same kinds of defects as studied for LaAlO₃ before are displayed in Fig. 5. In contrast to LaAlO₃, the bare SrTiO₃ slab as shown in Fig. 5(a) turns out to be an insulator with a band gap of about 1 eV, much smaller than the value of about 2 eV obtained for bulk SrTiO₃ with the same value of U for the Ti $3d$ orbitals.^{66,71} According to additional calculations with varying numbers of layers in the SrTiO₃ slab we concluded that the minimum number of unit cells required to reproduce bulk electronic properties is four, which led us to use $4\frac{1}{2}$ unit cells of SrTiO₃ in the central region of the LaAlO₃/SrTiO₃/LaAlO₃ heterostructure slab to be

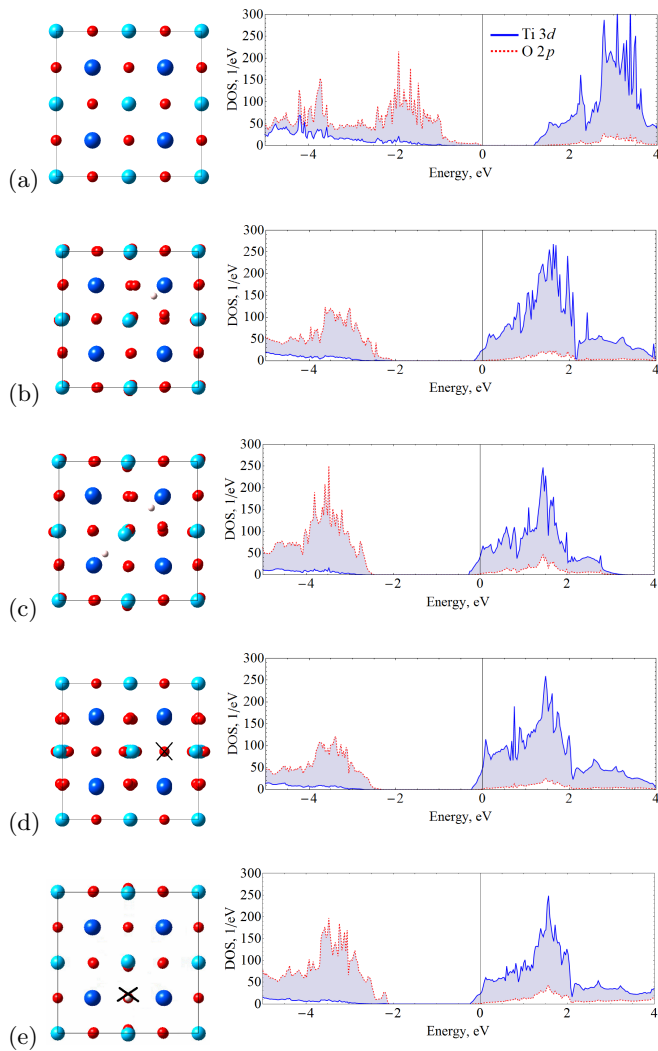


FIG. 5: Left column: top views of (a) bare 2×2 SrTiO₃ surface as well as a surface with (b) one hydrogen atom, (c) two hydrogen atoms, (d) an oxygen vacancy, and (e) an oxygen vacancy filled with a hydrogen atom. Strontium, titanium, oxygen, and hydrogen atoms are given in dark blue, light blue, red, and light grey, respectively, whereas oxygen vacancies are marked by a cross. Right column: Corresponding partial electronic densities of states.

discussed in the following subsection.

Eventually, the insulating nature of the SrTiO₃ slab can be traced back to the fact that, in contrast to LaAlO₃, within an ionic picture the alternating TiO₂ and SrO layers are both neutral since all atomic shells can be filled within each layer separately. As a consequence, a {001} surface does not induce any missing charge or charge transfer and thus within the ionic picture the electronic state is the same as in the bulk material.

Figs. 5(b) to 5(e) reveal the influence of defects on the structural and electronic properties of the slab. All kinds of defects taken into consideration cause atomic relaxations as well as a strong upshift of the Fermi en-

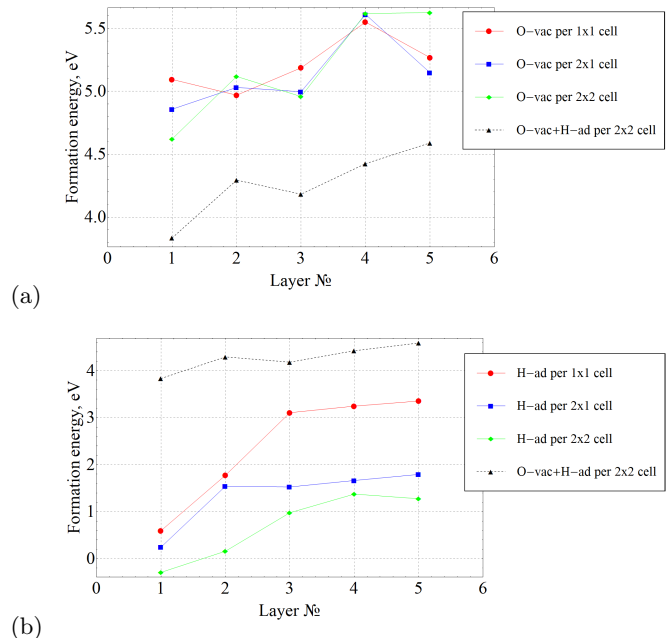


FIG. 6: Defect formation energies of TiO₂-terminated SrTiO₃ slabs (a) with an oxygen vacancy and (b) with a hydrogen dopant atom in dependence of the position of the defect. Layer 1 is the surface layer and counting of layers treats SrO and TiO₂ layers separately.

ergy with a finite occupation of the lowest conduction band states of one electron in the case of one hydrogen adatom (Fig. 5(b)) or an oxygen vacancy filled with hydrogen (Fig. 5(e)) per 2×2 supercell. In contrast, for two hydrogen adatoms (Fig. 5(c)) or a single oxygen vacancy (Fig. 5(d)) the conduction-band occupations rise to two.

Calculated energies of defect formation for different kinds of defects at various concentrations and at different positions are displayed in Fig. 6. As before, the curve for the case of an oxygen vacancy filled with a single hydrogen atom is included in both subfigures and serves as an orientation. For hydrogen dopant atoms the general trends are very similar to those already observed for the LaAlO₃ slabs. However, there is in general an upshift of all curves leaving only the case of a single surface hydrogen atom per 2×2 surface unit cell with a negative energy of formation.

The situation is much different for oxygen vacancies. Even though they show an overall increasing energy of formation at layers further away from the surface, the Coulomb repulsion between neighbouring vacancies seems to be considerably suppressed as compared to the situation in LaAlO₃ slabs. Specifically, for oxygen vacancies at the surface the difference in energy of defect formation between the lowest and highest concentration is 0.5 eV in SrTiO₃, whereas it amounts to about 4.3 eV in LaAlO₃. The tendency of increasing formation energy with layer depth and the larger and smaller spreads in

dependence on the layer was also observed in Ref. 86 and is similar in our work. It is not unreasonable to relate the reduction in the screening of the Coulomb repulsion between the charged defects to local correlations: recently, it was observed that increasing U on the La $4f$ orbitals of $\text{LaAlO}_3/\text{SrTiO}_3$ heterostructures reduces the lattice polarization within the LaO layers.^{42,66} With this in mind one may expect the least screening of the Coulomb repulsion for the layers with the strongest U . However such an argument is rather tentative and needs further analysis which is beyond the scope of this work.

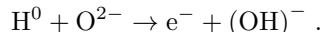
Finally, the values of defect formation energies for oxygen vacancies filled with a hydrogen dopant atom (dashed line in Fig. 6) lie between the formation energies of oxygen vacancies and hydrogen dopant atoms as expected and as also observed for LaAlO_3 .

C. $\text{LaAlO}_3/\text{SrTiO}_3/\text{LaAlO}_3$ slab

A two-dimensional metallic electron system is formed at the interface when at least four unit cells of LaAlO_3 (LAO) are grown on the TiO_2 -terminated SrTiO_3 (STO) substrate,^{7,9} which results in n -type doping of the interface. Concomitant p -type doping of the LaAlO_3 surface is expected from *ab initio* calculations^{89,90} for the defect-free LAO-STO heterostructure on account of the polar catastrophe mechanism⁸ but has not been observed experimentally.^{9,46}

A promising explanation for the suppression of the surface metallic state is a surface redox process, which leads to a release of bound electrons as free-carrier charges.^{51,52} The most relevant example of such a process is oxygen vacancy formation. These vacancies are the most discussed type of defects in the literature from both experimental^{22-24,91} and theoretical^{75,76,92} perspectives. Moreover, oxygen vacancies are considered to be responsible for the formation of magnetic order.^{16,19,20}

Usually, growth of $\text{LaAlO}_3/\text{SrTiO}_3$ heterostructures is complemented by a post-oxidation procedure at high pressures in order to reduce the amount of oxygen vacancies.⁹³ Such a treatment is accompanied by surface contamination with water, hydrocarbons, and H_2 amongst others; samples could be also contaminated during experiments or storage. As was demonstrated in some theoretical studies, such adsorbates can donate electrons to the interface.^{22,77,94} Bristowe *et al.* and Scheiderer *et al.* proposed a similar mechanism to explain additional charges due to atomic hydrogen adsorption,^{51,93} which can be understood from the reaction



The hydrogen atom bonds to the oxygen anion and therefore oxidizes under release of one electron per hydrogen atom. The electron moves to the interface resulting in an increase of the charge carrier density. In contrast, ionized hydrogen (H^+) cannot follow the same mechanism. The role of water and surface protonation was studied

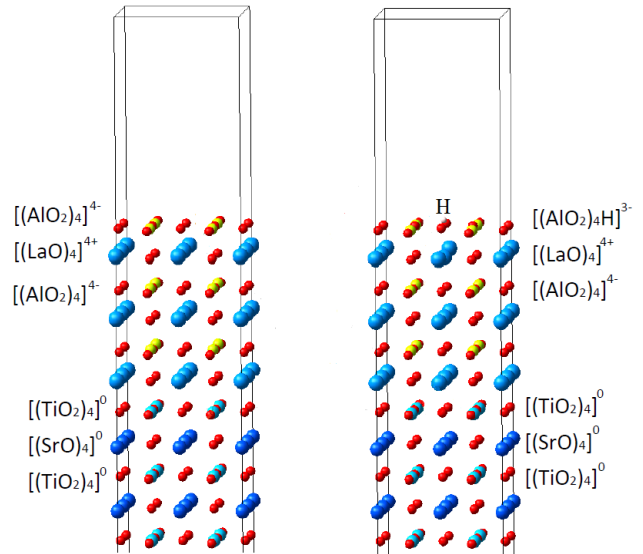


FIG. 7: Structures and ionic models of AlO_2 -terminated slabs of a $\text{LaAlO}_3/\text{SrTiO}_3$ heterostructure with three LAO overlayers. Both a bare slab (left) and a slab with one hydrogen adatom per 2×2 surface unit cell at the surface (right) are displayed. Only the upper part of the slab cell is shown.

also from the viewpoint of conductivity switching.⁹⁵ It was shown that protonation can lead to a fully reversible change of conductance by more than four orders of magnitude. Water coating was also used for writing and erasing nanostructures at the interface.⁹⁶

In the present work, we investigate the impact of defects (hydrogen dopants, oxygen vacancies as well as combination of these two) at various concentrations and various positions inside the LaAlO_3 and SrTiO_3 slabs on the structural and electronic properties. In particular, in the present section we demonstrate the influence of the aforementioned defects on the electronic properties of a $\text{LaAlO}_3/\text{SrTiO}_3$ heterostructure with three LaAlO_3 overlayers as displayed in Fig. 7.

Crystal structures of the bare heterostructure and heterostructures with different kinds of defects and the corresponding calculated partial densities of states are displayed in Fig. 8. Obviously, the bare heterostructure with three LaAlO_3 overlayers (Fig. 8(a)) has a band gap of about 0.6 eV. In contrast, all considered types of surface defects cause finite occupation of the Ti $3d$ states leading to metallic conductivity (see Figs. 8(b) to 8(e)). These findings are not at all obvious from the ionic picture so successfully used above, within which bulk LaAlO_3 can be considered as a sequence of negatively charged $(\text{AlO}_2)^-$ and positively charged $(\text{LaO})^+$ layers. That is, each LaO layer donates half an electron (per 1×1 surface unit cell) to the neighboring AlO_2 layers on both sides. The situation is different for LaAlO_3 overlayers grown on top of SrTiO_3 (and for polar LaAlO_3 slabs with an equal number of LaO and AlO_2 layers). Still, according to the ionic picture each LaO layer would

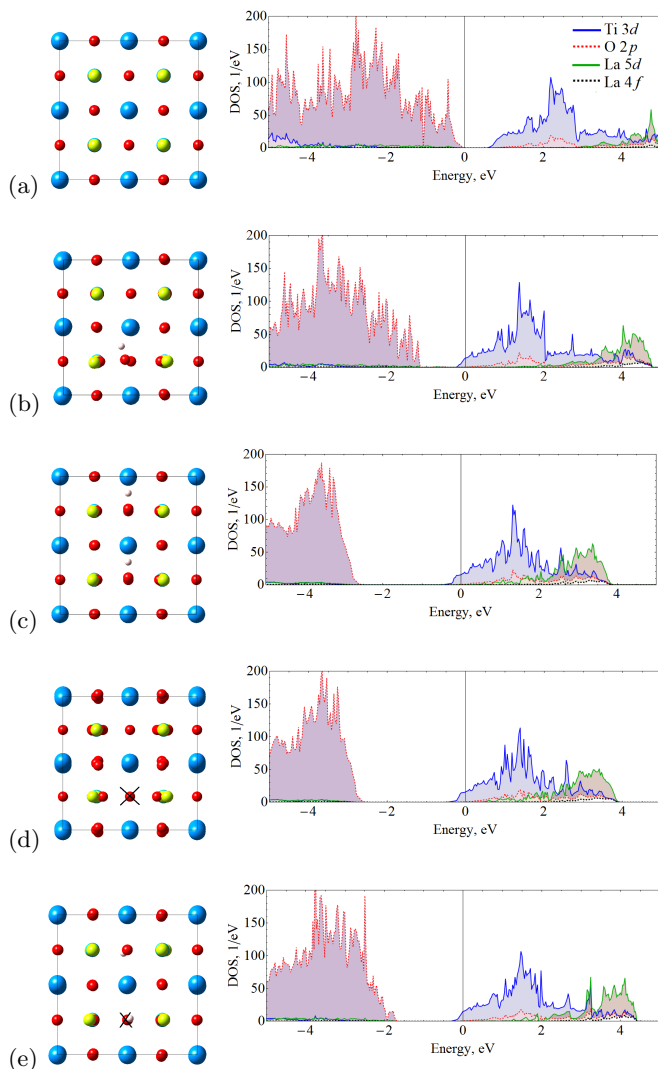


FIG. 8: Left column: top views of (a) bare 2×2 LaAlO₃-surface of an LaAlO₃/SrTiO₃ heterostructure, (b) with one hydrogen atom on the surface, (c) with two hydrogen atoms, (d) with one oxygen vacancy, and (e) with an oxygen vacancy filled with a hydrogen atom. Aluminum, lanthanum, oxygen, and hydrogen atoms are given in yellow, blue, red, and light grey, respectively, whereas oxygen vacancies are marked by a cross. Right column: Corresponding partial electronic densities of states.

donate one electron and each AlO₂ layer would receive one electron (per layer unit cell) in order to avoid partially occupied atomic shells. However, in a slab geometry this would eventually signify a potential built-up from one side of the overlayer to the other. Since this situation is energetically unstable for sufficiently thick LaAlO₃ overlayers, the oxygen states at the surface are not completely filled whereas the La 5d states at the interface are expected to be partially filled and metallic conductivity would arise in these two layers. In other words, both surfaces of the overlayer, i.e. both the interface with the neighboring TiO₂ layer and the AlO₂-

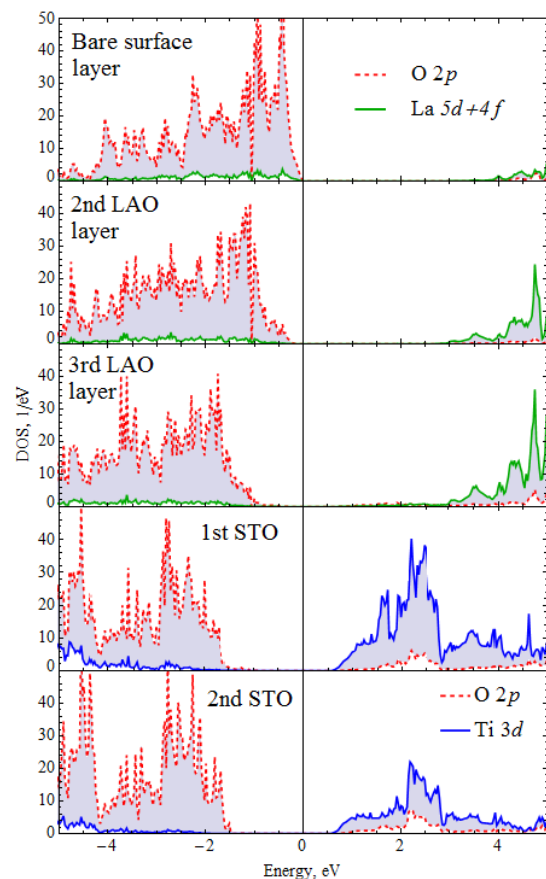


FIG. 9: Layer-resolved DOS for a 2×2 bare LaAlO₃/SrTiO₃ heterostructure.

terminated surface layer would become metallic whereby the charge carriers at the interface in fact reside in the Ti 3d states, not in the La 5d states. Again, this line of reasoning is the same for a polar LaAlO₃ slab. While this scenario is indeed obtained from calculations for un-relaxed structures, structural relaxation induces dipole fields in the LAO planes,^{90,97} which counteract the field from the polar setup, and thereby restore semiconducting behavior for LAO slabs below a critical thickness, as is indeed observed in Fig. 8(a) for the case of three LaAlO₃ overlayers.

Starting from the semiconducting state observed for the bare heterostructure with three overlayers, the defects considered here all introduce metallic conductivity at the interface. This may be induced by either two H-adatoms per 2×2 surface cell, see Fig. 8(c), or by an oxygen vacancy within the same surface unit cell, see Fig. 8(d). Both situations lead to a surface layer with formal charge -4 and occupation of the lowest part of the conduction band, which is of Ti 3d character.

It is very instructive to study the effect of hydrogen adatoms on the electronic structure by means of the layer-resolved densities of states. The corresponding results for the bare heterostructure and the heterostructure with two hydrogen atoms at the surface are shown

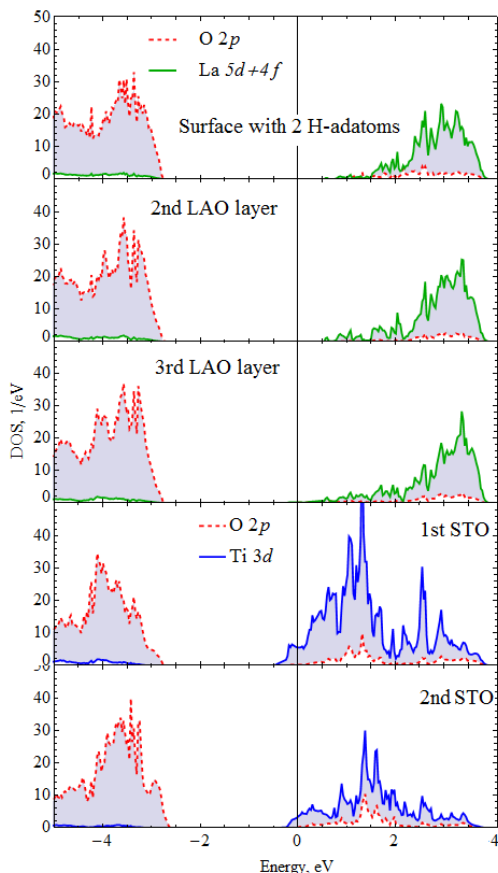


FIG. 10: Layer-resolved DOS for a 2×2 $\text{LaAlO}_3/\text{SrTiO}_3$ heterostructure with two hydrogen adatoms at its surface.

in Figs. 9 and 10, respectively. Note that these layer-resolved densities of states correspond to the densities of states displayed in Figs. 8(a) and 8(c), respectively. In Fig. 9 we clearly observe a downshift of the electronic states on going from the surface to the interface, which we attribute to the built-up of electric potential mentioned above. Indeed, this potential shift is clearly observed in Fig. 11, which displays the effective single-particle potential across the slab averaged over planes parallel to the surface. While for the bare heterostructure all layers are semiconducting as expected from the densities of states shown in Fig. 8(a), the metallic behavior of the heterostructure with hydrogen adatoms results from filling of the Ti $3d$ states at the interface, since the electrons provided by the H adatoms make charge transfer from the interface to the surface as observed for the bare heterostructure obsolete. At the interface the carriers are then attracted by the TiO_2 layer due to the higher electronegativity of Ti as compared to La and this causes the metallic conductivity in this layer. As a consequence of the reduced charge transfer across the LAO overlayers, the potential difference between surface and interfaces is considerably reduced as is indeed observed in Fig. 11 as well as in Fig. 10, where the valence band maximum formed from the O $2p$ states in the LAO overlayer stays

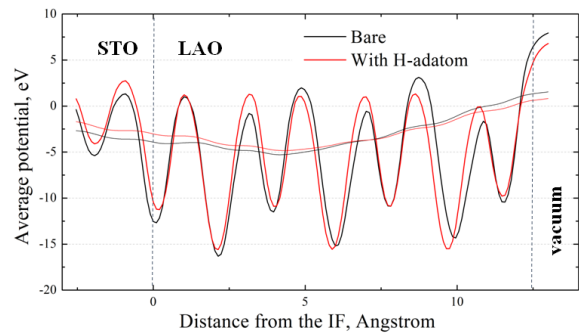


FIG. 11: Average effective single-particle potential of AlO_2 -terminated $\text{LaAlO}_3/\text{SrTiO}_3$ heterostructures with three LaAlO_3 overlayers. The black and red curve refer to the bare heterostructure and the heterostructure with two hydrogen surface adatoms per 2×2 surface cell, respectively, corresponding to the situations shown in Figs. 9 and 10. The smooth curves were generated from the original ones by proper broadening to allow for a better comparison of the overall trends.

at the same energetical position throughout the slab and also the lower edge of the La $5d$ states barely shifts.

The just outlined passivation of the surface by adsorption of hydrogen, which is equivalent to the situation of a surface with oxygen vacancies as sketched in Fig. 8(d) and in qualitative agreement with Refs. 51,52 thus naturally explains why no built-up of electric potential has been observed in experiments^{47–49} and at the same time the surface is insulating.^{9,49} However this does not yet explain the observation of a critical thickness of the LAO overlayer necessary to form a conducting interface, which we will address below.

Finally, for the case of one excess electron provided by one hydrogen adatom per 2×2 surface cell as presented in Fig. 8(b) and the equivalent situation of an oxygen vacancy filled by a hydrogen atom as displayed in Fig. 8(e) surface passivation is not complete and the just discussed effects become less pronounced but still cause metallic conductivity at the interface with a smaller filling of the Ti $3d$ states.

The formation energies calculated for various types of defects at various concentrations are displayed in Fig. 12. Here we also account for buried point defects by placing them in layers below the surface extending even into the STO substrate. For both hydrogen dopants and oxygen vacancies we observe increase of the formation energy with increasing concentration as a consequence of their Coulomb repulsion. In addition, formation energies generally are lowest for defects at the surface. However, especially formation energies of hydrogen dopants saturate beyond the second layer due to effective screening. This is different for oxygen vacancies, which show strong increase of the formation energies towards deeper LAO layers and show saturation only within the STO substrate. For higher concentrations this behavior leads even to a strong decrease of the formation energy between the fifth

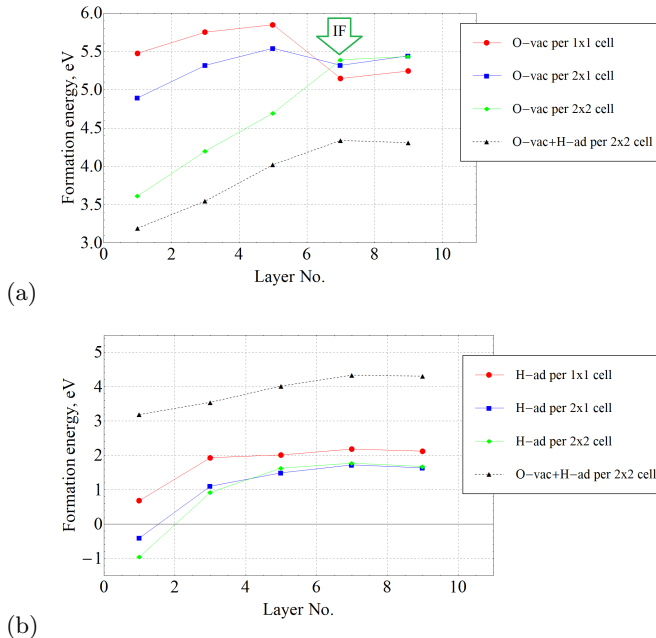


FIG. 12: Defect formation energies of AlO_2 -terminated $\text{LaAlO}_3/\text{SrTiO}_3$ heterostructures (a) with an oxygen vacancy and (b) with a hydrogen adatom in dependence of the position of the defect. Layer 1 is the surface layer and counting of layers treats LaO , AlO_2 , SrO and TiO_2 layers separately.

and seventh layer (counted from the surface) as was also observed for four LaAlO_3 overlayers.¹⁶ Nevertheless, according to these results only hydrogen adatoms at rather low concentration will form stable defect configurations, whereas all other defects show positive formation energies.

In passing we point to the value of about 0.7 eV found for the formation energy of a hydrogen adatom at the surface of a 1×1 surface cell, which agrees rather well with the value of about 0.5 eV given by Son and coworkers.⁷⁷

As mentioned before, the surface passivation scenario sketched above, while nicely explaining the suppression of the shift of both the effective potential and the band edges across the LAO overlayer as well as the semiconducting and metallic behavior of the surface and interface, respectively, does not yet provide an explanation for the onset of the latter situation observed at four LAO layers and beyond. In this context it is very helpful to consider the formation energy of hydrogen adatoms as a function of the number of LAO overlayers, which is displayed in Fig. 13. Note that the value of the defect formation energy for three LAO overlayers shown in this figure is identical to the value given for layer 1 for one hydrogen per 2×1 surface cell given in Fig. 12. Obviously, stable adsorption of hydrogen is unlikely for thin LAO overlayers and only at a critical thickness of the LAO slab do H adatoms form a stable connection with the surface, which eventually causes the metallic interface as

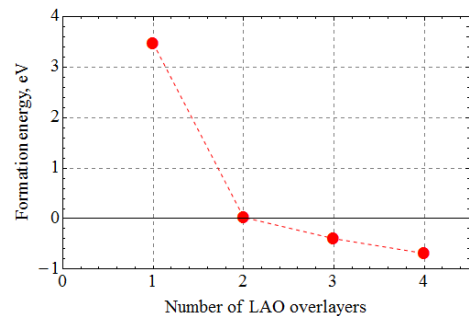


FIG. 13: Defect formation energies of AlO_2 -terminated $\text{LaAlO}_3/\text{SrTiO}_3$ heterostructures with one H adatom per 2×1 surface cell as a function of the number of LAO overlayers. Note that the data point for 3 LAO overlayers is identical to the blue data point for layer 1 in Fig. 12.

outlined above. For the investigated set-up this critical thickness is slightly above 2 LAO overlayers whereas experiments rather suggest a critical thickness between 3 and 4 LAO layers.⁹ However, the tendency to bind hydrogen at the surface of this heterostructure with increasing thickness of the LAO slab is clearly demonstrated in Fig. 13. Furthermore, note that according to Fig. 12 the formation energies depend somewhat on the defect concentration. We thus take this finding as a proof of principle for a critical thickness which eventually controls the transition to a metallic interface state through binding of surface adatoms. Similar conclusions have been drawn in Refs. 51–54, and our results qualitatively agree with those of Ref. 77 though there a 1×1 surface cell is taken.

IV. IMPACT OF IMPURITIES ON MAGNETIC PROPERTIES

As mentioned in the introduction, the origin of the magnetic order forming at the interface below room temperature,¹⁴ which coexists with a superconducting state below 300 mK,^{12,13} is still a matter of discussion.^{15–22} However, from *ab initio* calculations including either static (+ U)^{15,16} or dynamic (+DMFT)²⁰ correlations it was concluded that ferromagnetic order can be induced by oxygen vacancies, whereas the bare heterostructure would not show a magnetic instability. In particular, oxygen vacancies at the interface lead to an orbital reconstruction at adjacent Ti sites and generate a local spin polarization. Schemes to extend the analysis of local moment formation to intermediate and low oxygen vacancy concentrations have been investigated in Refs. 19 and 98.

While the previous studies dealt with heterostructures with four LAO overlayers, here we focus on 3LAO/STO heterostructures and consider the role of oxygen vacancies in the AlO_2 surface plane and in the TiO_2 interface plane for the onset of ferromagnetism by performing spin-polarized calculations. In addition, we investigate,

for the first time, the impact of hydrogen dopants on local-moment formation.

A. Oxygen vacancy

Being motivated by the nontrivial finding that for sufficiently large concentrations of oxygen vacancies the formation energy drops at the interface (see Fig. 12(a)) we reexplored the distinct orbital contributions of Ti atoms to the spin-resolved density of states. In doing so, we focused especially on two different scenarios, namely, in addition to the bare heterostructure, heterostructures with oxygen vacancies either in the surface AlO_2 layer or in the TiO_2 layer at the interface. The results of the corresponding spin-polarized calculations are displayed in Fig. 14. While the spin- and orbital-resolved $3d$ densities of states of all Ti atoms of the bare 3LAO/STO heterostructure as shown in Fig. 14(a) clearly reveal the insulating behaviour and zero magnetic moment of this situation, the presence of an oxygen vacancy at the surface causes an upshift of the Fermi energy and thus finite conductivity as has been already discussed in connection with Fig. 8(d). Here, we obtain, in addition, a finite spin-splitting especially of the Ti $3d t_{2g}$ states at the interface as becomes obvious from Fig. 14(b). In contrast, the Ti $3d e_g$ states, which are located at higher energies as expected from the octahedral arrangement of the O atoms about the Ti sites, experience a much smaller splitting. The total magnetic moment amounts to $0.50 \mu_B$ per full 2×2 cell, whereas the magnetic moment per single interface plane of $0.22 \mu_B$ underlines the confinement of the magnetic moment in this plane. Qualitatively, our results agree well with those of Refs. 15,16, which, however, were obtained for heterostructures with four LAO overlayers rather than the three-overlayer heterostructures studied in the present work.

The situation changes, when the vacancies are located in the interface TiO_2 layer. The resulting Ti $3d$ partial densities of states are displayed in Figs. 14(c) and 14(d), where we distinguish contributions from a distant Ti atom and a Ti atom next to the vacancy, respectively. Most striking is the downshift of the e_g states of the latter atom as compared to those of the former by about 2 eV, which leads to a finite occupation of these orbitals as well as a finite contribution to the local magnetic moment, which even exceeds that of the t_{2g} states. In contrast, the t_{2g} partial densities of states of both atoms are very similar. The calculated local magnetic moments are given in Fig. 15. They give rise to a magnetic moment of $0.65 \mu_B$ per single interface plane. In contrast, the adjacent layers carry negligible magnetic moments of $0.05 \mu_B$ within the 2×2 interface LaO layer, and $0.02 \mu_B$ and $0.03 \mu_B$ within the nearest SrO and TiO_2 layers, respectively. The total magnetic moment per 2×2 cell amounts to $1.54 \mu_B$. Hence, as for the case of a surface oxygen vacancy about 85% of the total magnetization is due to the layer comprising the vacancy. Moreover, va-

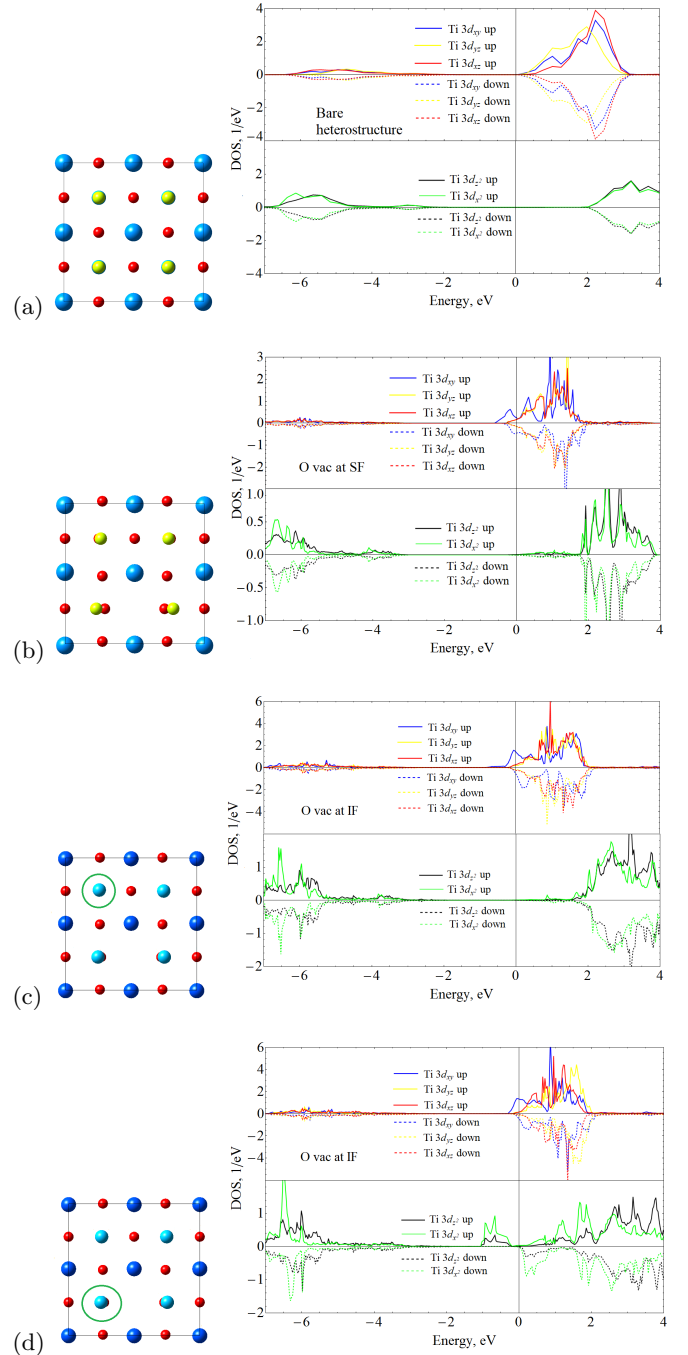


FIG. 14: Left column: top views of (a) bare 2×2 LaAlO_3 -surface of an $\text{LaAlO}_3/\text{SrTiO}_3$ heterostructure and with oxygen vacancy located in (b) the surface AlO_2 layer or (c)/(d) the interfacial TiO_2 layer. Aluminum, lanthanum, oxygen, strontium, titanium, and hydrogen atoms are given in yellow, blue, red, dark blue, light blue, and light grey, respectively, whereas oxygen vacancies are marked by a cross. Right column: Corresponding spin- and orbital-projected Ti $3d$ electronic densities of states of (a) all Ti atoms, (b) an interfacial Ti atom, (c) an interfacial Ti atom distant from the O vacancy and (d) an interfacial Ti atom close to the O vacancy.

cancies in the TiO_2 plane neighboring the interface plane

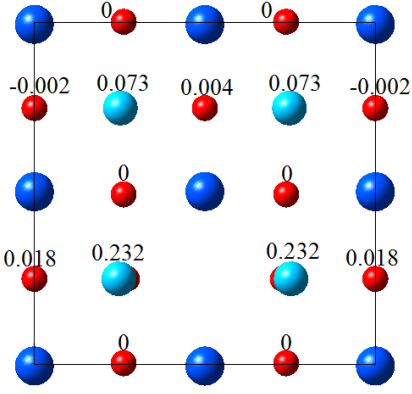


FIG. 15: Local moments of a 2×2 3LAO/4.5STO/3LAO heterostructure with one oxygen vacancy located at each of the interfaces. Strontium, titanium, and oxygen atoms are given in dark blue, light blue, and red, respectively.

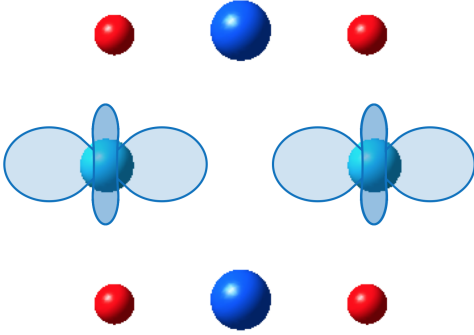


FIG. 16: Local cluster with an oxygen vacancy and two adjacent Ti atoms, cutout from Fig. 15. In this cluster the Ti $3de_g$ states with orbital lobes in the direction of the vacancy position are shifted below the Ti $3dt_{2g}$ states (“orbital reconstruction” [16]). The standard basis orbitals of the e_g states, i.e. the $d_{x^2-y^2}$ and $d_{3z^2-r^2}$ states, are rotated to produce $d_{y^2-z^2}$ and $d_{3x^2-r^2}$ states. The $d_{3x^2-r^2}$ orbitals, which have the lower energy and lobes in the direction of the vacancy, are delineated by a contour line. These orbitals carry a triplet state of the two charge-compensating electrons.

form a magnetic moment of only $0.16 \mu_B$.¹⁶ In the next-nearest neighboring TiO_2 plane a magnetic moment of approximately $0.08 \mu_B$ is identified and for vacancies in the third plane from the interface the magnetic moment is approximately zero. We thus arrive at the conclusion that oxygen vacancies at the interface induce atomically thin magnetic layers with a rather uniform background of magnetic moments generated by the Ti $3d t_{2g}$ states, which are complemented by well localized magnetic moments due to e_g states of the Ti atoms neighboring the vacancy. Of course, as is clear from the local geometry, the latter contributions can be even assigned to a single e_g orbital, namely, the one with its lobes pointing towards the vacancy (see Fig. 16). However, in the standard representation with the $3d_{x^2-y^2}$ and $3d_{3z^2-r^2}$ orbitals hav-

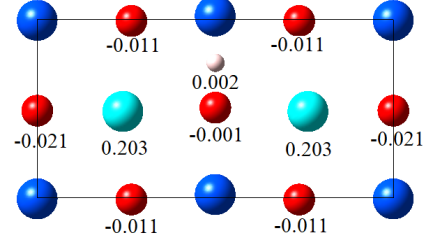


FIG. 17: Local moments of a 2×1 3LAO/4.5STO/3LAO heterostructure with a H dopant atom located at each of the interfaces. Strontium, titanium, oxygen and hydrogen atoms are given in dark blue, light blue, red, and light grey, respectively.

ing their lobes parallel and perpendicular, respectively, to the interface plane, this is not obvious from the partial densities of states. Nevertheless, the situation is not unlike that in V_2O_5 , which has a layered structure with VO_5 square pyramids rather than VO_6 octahedra as basic structural units leading to strong downshift of the V $3d_{xy}$ states due to reduced bonding-antibonding splitting and the formation of the characteristic split-off conduction band below about 1 eV the bottom of the other V $3d$ bands.⁹⁹ As before, we point to the good qualitative agreement of our results with the previous $+U$ and $+\text{DMFT}$ calculations, even though the latter, while accounting for quantum fluctuations, lead to considerably reduced magnetic moments.^{15,16,20}

B. Hydrogen dopants

Finally, spin-polarized calculations were also performed for a 2×1 supercell of the 3LAO/4.5STO/3LAO heterostructure with one hydrogen dopant located either in the AlO_2 surface layer or in the TiO_2 interface layer. Whereas the former case leads to a negligible magnetization, hydrogen dopants in the interface layer induce sizable magnetic moments. The calculated local magnetic moments are given in Fig. 17. Specifically, the magnetic moment per single TiO_2 layer amounts to $0.38 \mu_B$ (per 2×1 cell) giving rise to a total magnetic moment of $0.82 \mu_B$. Hence, the confinement of the magnetization to the layer holding the vacancy is even stronger than in the previous cases.

The spin-resolved Ti $3d$ partial densities of states are shown in Fig. 18. Obviously, contrasting the situation of an oxygen vacancy in the interface layer discussed in the previous section, no downshift of the Ti $3d e_g$ orbitals is observed since the octahedral environment of the metal atoms is not affected. Moreover, since, as shown in Fig. 17, the hydrogen dopant forms an almost rectangular triangle with the neighbouring Ti atoms in the same plane, its s -orbital hybridizes mainly with the Ti d_{xy} orbitals but much less with the d_{xz} and d_{yz} states. As a consequence, electron transfer from the H $1s$ orbital is

predominantly to the d_{xy} orbitals of the $3d t_{2g}$ manifolds centered at the neighboring Ti ions, which thus hold the large part of the local magnetic moment. In contrast, the d_{xz} and d_{yz} bands contribute only little to the magnetic moment as their occupation mainly results from overlap with adjacent layers of the interface.

Finally, we investigated the case of a hydrogen dopant atom filling an oxygen vacancy, which, however, again comes with a negligible magnetization.

V. SUMMARY

In the present work, first principles electronic structure calculations as based on density functional theory and including local electronic correlations within the GGA+ U approach have been employed to study the impact of oxygen vacancies and hydrogen dopant atoms on the electronic properties of slabs formed from LaAlO_3 (LAO) and SrTiO_3 (STO) as well as of LAO/STO/LAO heterostructure slabs. In particular, focus was on the insulating heterostructures with three LaAlO_3 overlayers. Both kinds of defects cause effective electron-type doping, which leads to metallic conductivity in the SrTiO_3 slab and the $\text{LaAlO}_3/\text{SrTiO}_3$ heterostructure, whereas the conductivity of LaAlO_3 slabs can be suppressed at suitable doping.

Calculated energies of defect formation show that hydrogen dopant atoms are more favorable at the surface than inside the slab for all structures and concentrations considered. The lowest formation energy was found for hydrogen adatoms at small concentrations (one hydrogen adatom per 2×2 supercell) due to the reduced Coulomb repulsion. However, note that in the present context we considered only the thermodynamic stability of defects, which still could be kinetically frozen even in case of positive defect formation energies.

Most strikingly, we find strong decrease of the formation energy of hydrogen adatoms on the surfaces of

LAO/STO heterostructures as the thickness of the LAO overlayer increases. In particular, this energy changes sign and becomes negative between two and three LAO overlayers for a defect concentration of two hydrogen adatoms per 2×2 surface cell. Taken together with the metallic conductivity induced by hydrogen dopant atoms, these findings would provide a consistent explanation for the semiconductor-metal transition observed for LAO/STO heterostructures at increasing thickness of the overlayers. The polar catastrophe mechanism without dopants has several drawbacks, as presented in Sec. I. Therefore, an alternative mechanism is of relevance, especially since the binding of H adatoms at the surface is thickness dependent and the critical thickness is a few LAO layers. Finally, the surface passivation scenario also explains the suppression of the shift of the effective potential across the LAO overlayer.

Contrasting the preference of hydrogen atoms for surface sites, the formation energies of oxygen vacancies develop local minima at the interface of LAO/STO heterostructures for high enough defect concentrations. Motivated by this finding as well as by previous reports that oxygen vacancies cause magnetism we confirmed the local-moment formation induced by vacancies located either at the surface or in the TiO_2 interface layer and found strong confinement of the magnetization within these layers. In addition, vacancies in the TiO_2 interface layer lead to drastic energetical downshift of the $3d e_g$ orbitals of the Ti atoms neighboring the vacancy, which carry large part of the well localized magnetic moment. Magnetism in the interface layer thus emerges from two distinct sources: While the Ti $3d t_{2g}$ orbitals form a rather uniform atomically thin background magnetization, the e_g orbitals of the Ti atoms neighboring the vacancy add point-like localized magnetic moments.

Finally, hydrogen dopant atoms in the TiO_2 interface layer of the LAO/STO heterostructure give rise to magnetism with even larger magnetic moments, which are mainly carried by the Ti $3d_{xy}$ states and again confined within the interface layer.

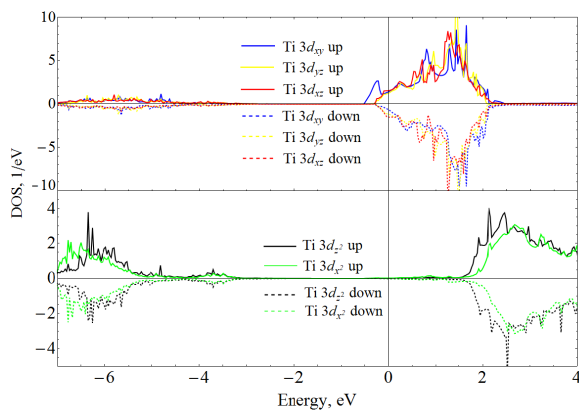


FIG. 18: Spin-resolved Ti $3d$ partial densities of states for a 2×1 supercell of the 3 LAO/4.5 STO/3 LAO heterostructure with one hydrogen dopant atom located at the interface.

Acknowledgments

We thank Dirk Fuchs, Jochen Mannhart, and Michael Sing for stimulating discussions. The research was carried out using the equipment of the shared research facilities of HPC computing resources at Lomonosov Moscow State University. The authors from KFU acknowledge partial support by the Program of Competitive Growth of Kazan Federal University. The work of I. I. Piyanzina was funded by a subsidy allocated to Kazan Federal University for the state assignment in the sphere of scientific activities (project 3.9779.2017/8.9) and by the German Science Foundation (DFG) – grant number 107745057 – TRR 80. All authors are grateful for the support by the TRR 80. T. Kopp wants to express his gratitude to the late Natalia Pavlenko who understood so much of this

physics and who was a brilliant coworker.

- ¹ J. Mannhart and D. G. Schlom, *Science* **327**, 1607 (2010).
- ² P. Zubko, S. Gariglio, M. Gabay, P. Ghosez, and J.-M. Triscone, *Annu. Rev. Condens. Matter Phys.* **2**, 141 (2011).
- ³ M. Bibes, J. E. Villegas, and A. Barthélémy, *Adv. Phys.* **60**, 5 (2011).
- ⁴ R. Hesper, L. H. Tjeng, A. Heeres, and G. A. Sawatzky, *Phys. Rev. B* **62**, 16046 (2000).
- ⁵ S. Okamoto and A. J. Millis, *Nature* **428**, 630 (2004).
- ⁶ In fact, Hesper, Tjeng, Heeres, and Sawatzky⁴ coined the term *electronic reconstruction* in connection with the surface electronic structure associated with a polar surface termination: a valence change of the surface ions leads to a metallic surface and thereby avoids the divergence of the electronic potential on account of the polar surface termination. Here, we take the viewpoint of Okamoto and Millis⁵ to generalize the term *electronic reconstruction* to include all situations where the surface or interface electronic phase differs from that in the adjacent bulk materials.
- ⁷ A. Ohtomo and H. Y. Hwang, *Nature* **427**, 423 (2004).
- ⁸ N. Nakagawa, H. Y. Hwang, and D. A. Muller, *Nature Mater.* **5**, 204 (2006).
- ⁹ S. Thiel, G. Hammerl, A. Schmehl, C. W. Schneider, and J. Mannhart, *Science* **313**, 1942 (2006).
- ¹⁰ M. Sing, G. Berner, K. Goß, A. Müller, A. Ruff, A. Wetscherek, S. Thiel, J. Mannhart, S. A. Pauli, C. W. Schneider, P. R. Willmott, M. Gorgoi, F. Schäfers, and R. Claessen, *Phys. Rev. Lett.* **102**, 176805 (2009).
- ¹¹ N. Reyren, S. Thiel, A. D. Caviglia, L. Fitting Kourkoutis, G. Hammerl, C. Richter, C. W. Schneider, T. Kopp, A.-S. Rüetschi, D. Jaccard, M. Gabay, D. A. Muller, J.-M. Triscone, and J. Mannhart, *Science* **317**, 1196 (2007).
- ¹² J. A. Bert, B. Kalisky, C. Bell, M. Kim, Y. Hikita, H. Y. Hwang, and K. A. Moler, *Nature Phys.* **7**, 767 (2011).
- ¹³ Lu Li, C. Richter, J. Mannhart, and R. Ashoori, *Nature Phys.* **7**, 762 (2011).
- ¹⁴ A. Brinkman, M. Huijben, M. Van Zalk, J. Huijben, U. Zeitler, J. C. Maan, W. G. van der Wiel, G. Rijnders, D. H. A. Blank, and H. Hilgenkamp, *Nature Mater.* **6**, 493 (2007).
- ¹⁵ N. Pavlenko, T. Kopp, E. Y. Tsymbal, G. A. Sawatzky, and J. Mannhart, *Phys. Rev. B* **85**, 020407(R) (2012).
- ¹⁶ N. Pavlenko, T. Kopp, E. Y. Tsymbal, J. Mannhart, and G. A. Sawatzky, *Phys. Rev. B* **86**, 064431 (2012).
- ¹⁷ K. Michaeli, A. C. Potter, and P. A. Lee, *Phys. Rev. Lett.* **108**, 117003 (2012).
- ¹⁸ B. Kalisky, J. A. Bert, B. B. Klopfer, C. Bell, H. K. Sato, M. Hosoda, Y. Hikita, H. Y. Hwang, and K. A. Moler, *Nature Commun.* **3**, 922 (2012).
- ¹⁹ N. Pavlenko, T. Kopp, and J. Mannhart, *Phys. Rev. B* **88**, 201104(R) (2013).
- ²⁰ F. Lechermann, L. Boehnke, D. Grieger, and C. Piefke, *Phys. Rev. B* **90**, 085125 (2014).
- ²¹ J. Ruhman, A. Joshua, S. Ilani, and E. Altman, *Phys. Rev. B* **90**, 125123 (2014).
- ²² L. Yu and A. Zunger, *Nature Commun.* **5**, 5118 (2014).
- ²³ J. Park, B.-G. Cho, K. D. Kim, J. Koo, H. Jang, K.-T. Ko, J.-H. Park, K.-B. Lee, J.-Y. Kim, D. R. Lee, C. A. Burns, S. S. A. Seo, and H. N. Lee, *Phys. Rev. Lett.* **110**, 017401 (2013).
- ²⁴ M. Salluzzo, S. Gariglio, D. Stornaiuolo, V. Sessi, S. Rusponi, C. Piamonteze, G. M. De Luca, M. Minola, D. Marré, A. Gadaleta, H. Brune, F. Nolting, N. B. Brookes, and G. Ghiringhelli, *Phys. Rev. Lett.* **111**, 087204 (2013).
- ²⁵ S. Banerjee, O. Erten, and M. Randeria, *Nature Phys.* **9**, 626 (2013).
- ²⁶ A. D. Caviglia, M. Gabay, S. Gariglio, N. Reyren, C. Cancellieri, and J.-M. Triscone, *Phys. Rev. Lett.* **104**, 126803 (2010).
- ²⁷ Z. Zhong, A. Tóth, and K. Held, *Phys. Rev. B* **87**, 161102 (2013).
- ²⁸ A. Joshua, J. Ruhman, S. Pecker, E. Altman, and S. Ilani, *Proc. Natl. Acad. Sci. USA* **110**, 9633 (2013).
- ²⁹ M. Ben Shalom, C. W. Tai, Y. Lereah, M. Sachs, E. Levy, D. Rakhmilevitch, A. Palevski, and Y. Dagan, *Phys. Rev. B* **80**, 140403(R) (2009).
- ³⁰ D. Fuchs, A. Sleem, R. Schäfer, A.G. Zaitsev, M. Mefert, D. Gerthsen, R. Schneider, and H. von Löhneysen, *Phys. Rev. B* **92**, 155313 (2015).
- ³¹ P. Seiler, J. Zabaleta, R. Wanke, J. Mannhart, T. Kopp, and D. Braak, *Phys. Rev. B* **97**, 075136 (2018).
- ³² L. Fidkowski, H.-C. Jiang, R. M. Lutchyn, and C. Nayak, *Phys. Rev. B* **87**, 014436 (2013).
- ³³ F. Loder, A. P. Kampf, and T. Kopp, *Sci. Rep.* **5**, 15302 (2015).
- ³⁴ M. S. Scheurer and J. Schmalian, *Nature Commun.* **6**, 6005 (2015).
- ³⁵ L. Kuerten, C. Richter, N. Mohanta, T. Kopp, A. Kampf, J. Mannhart, and H. Boschker *Phys. Rev. B* **96**, 014513 (2017).
- ³⁶ Lu Li, C. Richter, S. Paetel, T. Kopp, J. Mannhart, and R. C. Ashoori, *Science* **332**, 825 (2011).
- ³⁷ K. Steffen, R. Frésard, and T. Kopp, *Phys. Rev. B* **95**, 035143 (2017).
- ³⁸ J. K. Freericks, *Transport in Multilayered Nanostructures*, 2nd edition, Imperial College Press (2016).
- ³⁹ S. Caprara, F. Peronaci, and M. Grilli, *Phys. Rev. Lett.* **109**, 196401 (2012).
- ⁴⁰ K. Steffen, F. Loder, and T. Kopp, *Phys. Rev. B* **91**, 075415 (2015).
- ⁴¹ N. Scopigno, D. Bucheli, S. Caprara, J. Biscaras, N. Bergeal, J. Lesueur, and M. Grilli, *Phys. Rev. Lett.* **116**, 026804 (2016).
- ⁴² J. Zabaleta, V. S. Borisov, R. Wanke, H. O. Jeschke, S. C. Parks, B. Baum, A. Teker, T. Harada, K. Syassen, T. Kopp, N. Pavlenko, R. Valentí, and J. Mannhart, *Phys. Rev. B* **93**, 235117 (2016).
- ⁴³ A. Raslan and W. A. Atkinson, *Phys. Rev. B* **98**, 195447 (2018).
- ⁴⁴ B. Förg, C. Richter, and J. Mannhart, *Appl. Phys. Lett.* **100**, 053506 (2012).
- ⁴⁵ J. Goniakowski, F. Finocchi, and C. Noguera, *Rep. Prog. Phys.* **71**, 016501 (2008).
- ⁴⁶ G. Berner, M. Sing, H. Fujiwara, A. Yasui, Y. Saitoh,

- A. Yamasaki, Y. Nishitani, A. Sekiyama, N. Pavlenko, T. Kopp, C. Richter, J. Mannhart, S. Suga, and R. Claessen, *Phys. Rev. Lett.* **110**, 247601 (2013).
- ⁴⁷ Y. Segal, J. H. Ngai, J. W. Reiner, F. J. Walker, and C. H. Ahn, *Phys. Rev. B* **80**, 241107(R) (2009).
- ⁴⁸ E. Slooten, Z. Zhong, H. J. A. Molegraaf, P. D. Eerkes, S. de Jong, F. Masee, E. van Heumen, M. K. Kruijze, S. Wenderich, J. E. Kleibeuker, M. Gorgoi, H. Hilgenkamp, A. Brinkman, M. Huijben, G. Rijnders, D. H. A. Blank, G. Koster, P. J. Kelly, and M. S. Golden, *Phys. Rev. B* **87**, 085128 (2013).
- ⁴⁹ G. Berner, A. Müller, F. Pfaff, J. Walde, C. Richter, J. Mannhart, S. Thiess, A. Gloskovskii, W. Drube, M. Sing, and R. Claessen, *Phys. Rev. B* **88**, 115111 (2013).
- ⁵⁰ D. Fuchs, R. Schäfer, A. Sleem, R. Schneider, R. Thelen, and H. von Löhneysen, *Appl. Phys. Lett.* **105**, 092602 (2014).
- ⁵¹ N. C. Bristowe, P. B. Littlewood, and E. Artacho, *Phys. Rev. B* **83**, 205405 (2011).
- ⁵² A. Janotti, L. Bjaalie, L. Gordon, and C. G. Van de Walle, *Phys. Rev. B* **86**, 241108 (2012).
- ⁵³ N. C. Bristowe, P. Ghosez, P. B. Littlewood, and E. Artacho, *J. Phys.: Condens. Matter* **26**, 143201 (2014).
- ⁵⁴ K. Krishnaswamy, C. E. Dreyer, A. Janotti, and C. G. Van de Walle, *Phys. Rev. B* **92**, 085420 (2015).
- ⁵⁵ P. Hohenberg and W. Kohn, *Phys. Rev.* **136**, B864 (1964).
- ⁵⁶ W. Kohn and L. J. Sham, *Phys. Rev.* **140**, A1133 (1965).
- ⁵⁷ J. P. Perdew, K. Burke, and M. Ernzerhof, *Phys. Rev. Lett.* **77**, 3865 (1996).
- ⁵⁸ P. E. Blöchl, *Phys. Rev. B* **50**, 17953 (1994).
- ⁵⁹ G. Kresse, and J. Furthmüller, *Comp. Mat. Sci.* **6**, 15 (1996).
- ⁶⁰ G. Kresse, and J. Furthmüller, *Phys. Rev. B* **54**, 11169 (1996).
- ⁶¹ G. Kresse, and D. Joubert, *Phys. Rev. B* **59**, 1758 (1999).
- ⁶² MedeA[®]-2.20, Materials Design, Inc., San Diego, CA, USA (2015).
- ⁶³ H. J. Monkhorst and J. D. Pack, *Phys. Rev. B* **13**, 5188 (1976).
- ⁶⁴ P. E. Blöchl, O. Jepsen, and O. K. Andersen, *Phys. Rev. B* **49**, 16223 (1994).
- ⁶⁵ S. L. Dudarev, G. A. Botton, S. Y. Savrasov, C. J. Humphreys, and A. P. Sutton, *Phys. Rev. B* **57**, 1505 (1998).
- ⁶⁶ I. I. Piyanzina, T. Kopp, Yu. V. Lysogorskiy, D. Tayurskii, and V. Eyert, *J. Phys.: Condens. Matter* **29**, 095501 (2017).
- ⁶⁷ M. Breitschaft, V. Tinkl, N. Pavlenko, S. Paetel, C. Richter, J. R. Kirtley, Y. C. Liao, G. Hammerl, V. Eyert, T. Kopp, and J. Mannhart, *Phys. Rev. B* **81**, 153414 (2010).
- ⁶⁸ F. Cossu, U. Schwingenschlögl, and V. Eyert, *Phys. Rev. B* **88**, 045119 (2013).
- ⁶⁹ F. Lin, S. Wang, F. Zheng, G. Zhou, J. Wu, B.-L. Gu, and W. Duan, *Phys. Rev. B* **79**, 035311 (2009).
- ⁷⁰ K. Krishnaswamy, C. E. Dreyer, A. Janotti, and C. G. Van de Walle, *Phys. Rev. B* **90**, 235436 (2014).
- ⁷¹ I. I. Piyanzina, Yu. V. Lysogorskiy, I. I. Varlamova, A. G. Kiiamov, T. Kopp, V. Eyert, O. V. Nedopekin, and D. A. Tayurskii, *J. Low Temp. Phys.* **185**, 597 (2016).
- ⁷² S. B. Zhang and J. E. Northrup, *Phys. Rev. Lett.* **67**, 2339 (1991).
- ⁷³ K. Reuter and M. Scheffler, *Phys. Rev. B* **65**, 035406 (2001); *Phys. Rev. B* **75**, 049901(E) (2007).
- ⁷⁴ C. Freysoldt, B. Grabowski, T. Hickel, J. Neugebauer, G. Kresse, A. Janotti, and C. G. Van de Walle, *Rev. Mod. Phys.* **86**, 253 (2014).
- ⁷⁵ Y. Li, S. N. Phattalung, S. Limpijumnong, J. Kim, and J. Yu, *Phys. Rev. B* **84**, 245307 (2011).
- ⁷⁶ L. Zhang, X.-F. Zhou, H.-T. Wang, J.-J. Xu, J. Li, E. G. Wang, and S.-H. Wei, *Phys. Rev. B* **82**, 125412 (2010).
- ⁷⁷ W.-J. Son, E. Cho, J. Lee, and S. Han, *J. Phys.: Condens. Matter* **22**, 315501 (2010).
- ⁷⁸ A. R. Silva and G. M. Dalpian, *J. Alloys Compd.* **684**, 544 (2016).
- ⁷⁹ C. Y. Thai, T. L. Wu, and A. Chin, *IEEE Electron Device Lett.* **33**, 35 (2012).
- ⁸⁰ P. C. McIntyre and M. J. Cima, *J. Mater. Res.* **9**, 2219 (1994).
- ⁸¹ Z. L. Wang and J. Zhang, *Phys. Rev. B* **54**, 1153 (1996).
- ⁸² W. Chen, L. Li, J. Qi, Y. Wang, and Z. Gui, *J. Am. Ceram. Soc.* **81**, 2751 (1998).
- ⁸³ A. F. Santander-Syro, O. Copie, and T. Kondo, F. Fortuna, S. Pailhès, R. Weht, X. G. Qiu, F. Bertran, A. Nicolaou, A. Taleb-Ibrahimi, P. Le Fèvre, G. Herranz, M. Bibes, N. Reyren, Y. Apertet, P. Lecocq, A. Barthélémy, and M. J. Rozenberg, *Nature* **469**, 189 (2011).
- ⁸⁴ W. Meevasana, P. D. C. King, R. H. He, S.-K. Mo, M. Hashimoto, A. Tamai, P. Songsirittthigul, F. Baumberger, and Z.-X. Shen, *Nat. Mater.* **10**, 114 (2011).
- ⁸⁵ J. Shen, H. Lee, R. Valentí, and H. O. Jeschke, *Phys. Rev. B* **86**, 195119 (2012).
- ⁸⁶ A. R. Silva and G. M. Dalpian, *J. Appl. Phys.* **115**, 033710 (2014).
- ⁸⁷ F. Lechermann, H. O. Jeschke, A. J. Kim, S. Backes, and R. Valentí, *Phys. Rev. B* **92**, 121103(R) (2016).
- ⁸⁸ L. Dudy, M. Sing, P. Scheiderer, J. D. Denlinger, P. Schütz, J. Gabel, M. Buchwald, C. Schlueter, T.-L. Lee, and R. Claessen, *Adv. Mater.* **28**, 7443 (2016).
- ⁸⁹ J. Lee and A. A. Demkov, *Phys. Rev. B* **78**, 193104 (2008).
- ⁹⁰ R. Pentcheva, W. E. Pickett, *Phys. Rev. Lett.* **102**, 107602 (2009).
- ⁹¹ A. Kalabukhov, R. Gunnarsson, J. Börjesson, E. Olsson, T. Claesson, and D. Winkler, *Phys. Rev. B* **75**, 121404 (2007).
- ⁹² Z. Zhong, P. X. Xu, P. J. Kelly, *Phys. Rev. B* **82**, 165127 (2010).
- ⁹³ P. Scheiderer, F. Pfaff, J. Gabel, M. Kamp, M. Sing, and R. Claessen, *Phys. Rev. B* **92**, 195422 (2015).
- ⁹⁴ Y. Li and J. Yu, *J. Phys.: Condens. Matter* **25**, 265004 (2013).
- ⁹⁵ K. A. Brown, S. He, D. J. Eichelsdoerfer, M. Huang, I. Levy, H. Lee, S. Ryu, P. Irvin, J. Mendez-Arroyo, C.-B. Eom, C. A. Mikrin, and J. Levy, *Nature Commun.* **7**, 10681 (2016).
- ⁹⁶ F. Bi, D. F. Bogorin, C. Cen, C. W. Bark, J.-W. Park, C.-B. Eom, and J. Levy, *Appl. Phys. Lett.* **97**, 173110 (2010).
- ⁹⁷ N. Pavlenko and T. Kopp, *Surf. Sci.* **605**, 1114 (2011).
- ⁹⁸ M. Behrmann and F. Lechermann, *Phys. Rev. B* **92**, 125148 (2015).
- ⁹⁹ V. Eyert and K.-H. Höck, *Phys. Rev. B* **57**, 12727 (1998).